

23. PASSAGE OF PARTICLES THROUGH MATTER

Revised May 1998 by D.E. Groom (LBNL).

23.1. Notation

Table 23.1: Summary of variables used in this section. The kinematic variables β and γ have their usual meanings.

Symbol	Definition	Units or Value
α	Fine structure constant	1/137.035 989 5(61)
M	Incident particle mass	MeV/ c^2
E	Incident particle energy $\gamma M c^2$	MeV
T	Kinetic energy	MeV
$m_e c^2$	Electron mass $\times c^2$	0.510 999 06(15) MeV
r_e	Classical electron radius $e^2/4\pi\epsilon_0 m_e c^2$	2.817 940 92(38) fm
N_A	Avogadro's number	$6.022 136 7(36) \times 10^{23}$ mol $^{-1}$
ze	Charge of incident particle	
Z	Atomic number of medium	
A	Atomic mass of medium	g mol $^{-1}$
K/A	$4\pi N_A r_e^2 m_e c^2/A$	0.307 075 MeV g $^{-1}$ cm 2 for $A = 1$ g mol $^{-1}$
I	Mean excitation energy	eV
δ	Density effect correction to ionization energy loss	
$\hbar\omega_p$	Plasma energy $\sqrt{4\pi N_e r_e^3} m_e c^2/\alpha$	28.816 $\sqrt{\rho(Z/A)}$ eV $^{(a)}$
N_e	Electron density	(units of r_e) $^{-3}$
w_j	Weight fraction of the j th element in a compound or mixture	
n_j	\times number of j th kind of atoms in a compound or mixture	
X_0	Radiation length	g cm $^{-2}$
—	$4\alpha r_e^2 N_A/A$	(716.408 g cm $^{-2}$) $^{-1}$ for $A = 1$ g mol $^{-1}$
E_c	Critical energy	MeV
E_s	Scale energy $\sqrt{4\pi/\alpha} m_e c^2$	21.2052 MeV
R_M	Molière radius	MeV g $^{-1}$ cm 2

(a) For ρ in g cm $^{-3}$.

23.2. Ionization energy loss by heavy particles [1–5]

Moderately relativistic charged particles other than electrons lose energy in matter primarily by ionization. The mean rate of energy loss (or stopping power) is given by the Bethe-Bloch equation,

$$-\frac{dE}{dx} = K z^2 \frac{Z}{A} \frac{1}{\beta^2} \left[\frac{1}{2} \ln \frac{2m_e c^2 \beta^2 \gamma^2 T_{\max}}{I^2} - \beta^2 - \frac{\delta}{2} \right]. \quad (23.1)$$

Here T_{\max} is the maximum kinetic energy which can be imparted to a free electron in a single collision, and the other variables are defined in Table 23.1. The units are chosen so that dx is measured in mass per unit area, *e.g.*, in g cm $^{-2}$.

In this form, the Bethe-Bloch equation describes the energy loss of pions in a material such as copper to about 1% accuracy for energies between about 6 MeV and 6 GeV. At lower energies corrections for tightly-bound atomic electrons and other effects must be made, and at higher energies radiative effects begin to be important. These limits of validity depend on both the effective atomic number of the absorber and the mass of the slowing particle. Low-energy effects will be discussed in Sec. 23.2.2.

The function as computed for pions on copper is shown by the solid curve in Fig. 23.1, and for pions on other materials in Fig. 23.2. A minor dependence on M at the highest energies is introduced through T_{\max} , but for all practical purposes in high-energy physics dE/dx in a given material is a function only of β . Except in hydrogen, particles of the same velocity have very similar rates of energy loss in different materials; there is a slow decrease in the rate of energy loss with increasing Z . The qualitative difference in stopping power behavior at high energies between a gas (He) and the other materials shown in Fig. 23.2 is due to the density-effect correction, δ , discussed below.

The stopping power functions are characterized by broad minima whose position drops from $\beta\gamma = 3.5$ to 3.0 as Z goes from 7 to 100.

In practical cases, most relativistic particles (*e.g.*, cosmic-ray muons) have energy loss rates close to the minimum, and are said to be minimum ionizing particles, or mip's.

Eq. (23.1) may be integrated to find the total range R for a particle which loses energy only through ionization. Since dE/dx depends only on β , R/M is a function of E/M or pc/M . In practice, range is a useful concept only for low-energy hadrons ($R \lesssim \lambda_I$, where λ_I is the nuclear interaction length), and for muons below a few hundred GeV (above which radiative effects dominate). R/M as a function of $\beta\gamma = pc/M$ is shown for a variety of materials in Fig. 23.3.

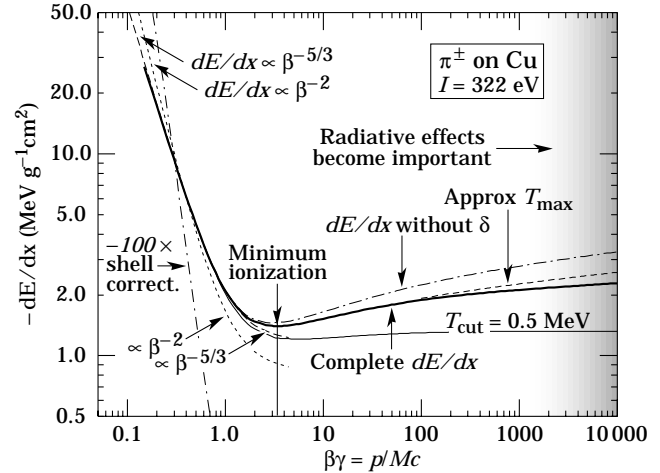


Figure 23.1: Energy loss rate in copper. The function without the density-effect correction, δ , is also shown, as is the loss rate excluding energy transfers with $T > 0.5$ MeV. The shell correction is indicated. The conventional β^{-2} low-energy approximation is compared with $\beta^{-5/3}$.

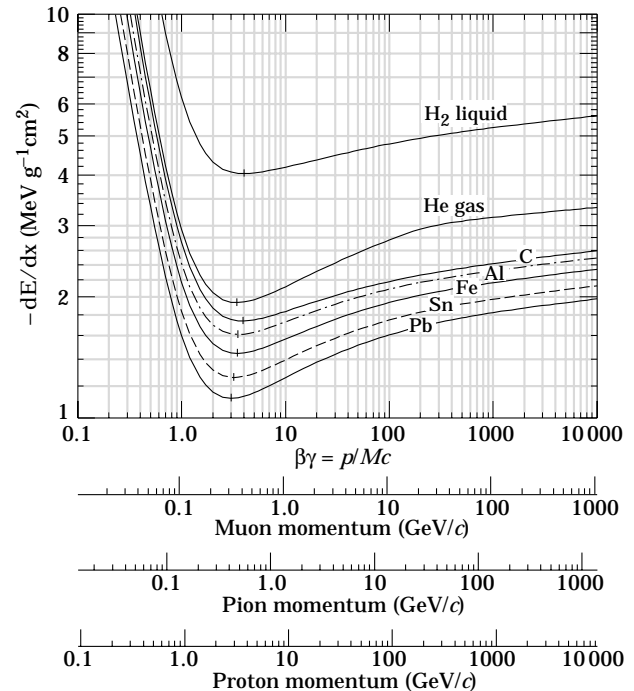


Figure 23.2: Energy loss rate in liquid (bubble chamber) hydrogen, gaseous helium, carbon, aluminum, tin, and lead.

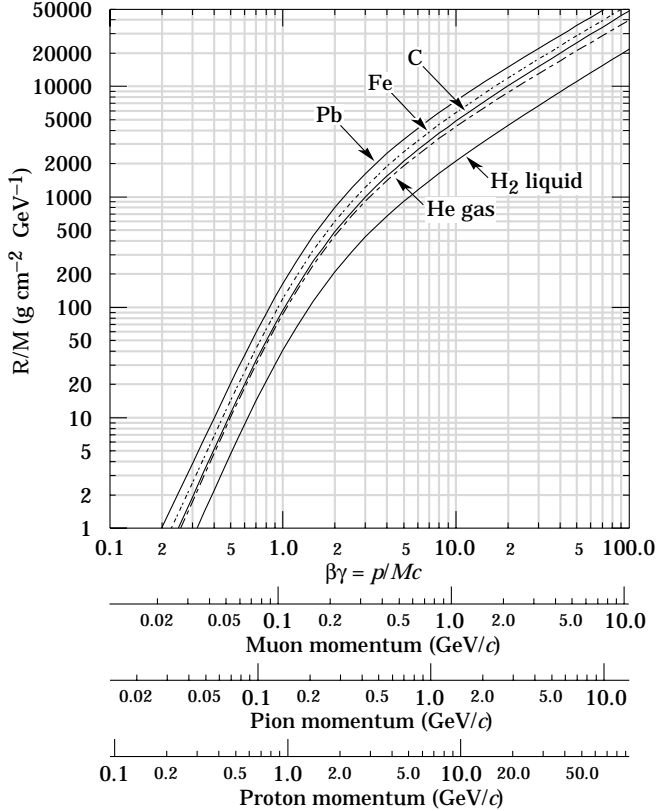


Figure 23.3: Range of heavy charged particles in liquid (bubble chamber) hydrogen, helium gas, carbon, iron, and lead. For example: For a K^+ whose momentum is 700 MeV/c, $\beta\gamma = 1.42$. For lead we read $R/M \approx 396$, and so the range is 195 g cm^{-2} .

For a particle with mass M and momentum $M\beta\gamma c$, T_{\max} is given by

$$T_{\max} = \frac{2m_e c^2 \beta^2 \gamma^2}{1 + 2\gamma m_e/M + (m_e/M)^2}. \quad (23.2)$$

It is usual [1,2] to make the “low-energy” approximation $T_{\max} = 2m_e c^2 \beta^2 \gamma^2$, valid for $2\gamma m_e/M \ll 1$; this, in fact, is done implicitly in many standard references. For a pion in copper, the error thus introduced into dE/dx is greater than 6% at 100 GeV. The correct expression should be used.

At energies of order 100 GeV, the maximum 4-momentum transfer to the electron can exceed 1 GeV/c, where structure effects significantly modify the cross sections. This problem has been investigated by J.D. Jackson [6], who concluded that for hadrons (but not for large nuclei) corrections to dE/dx are negligible below energies where radiative effects dominate. While the cross section for rare hard collisions is modified, the average stopping power, dominated by many softer collisions, is almost unchanged.

The mean excitation energy I is $(10 \pm 1 \text{ eV}) \times Z$ for elements heavier than sulphur. The values adopted by the ICRU for the chemical elements [7] are now in wide use; these are shown in Fig. 23.4. Machine-readable versions can also be found [8]. Given the availability of these constants and their variation with atomic structure, there seems little point to depending upon approximate formulae, as was done in the past.

Ionization losses by electrons and positrons [7,9,10] are not discussed here. Above the critical energy, which is a few tens of MeV in most materials (see Fig. 23.7), bremsstrahlung is the dominant source of energy loss. This important case is discussed below. The contributions of various electron energy-loss processes in lead are shown in Fig. 24.4.

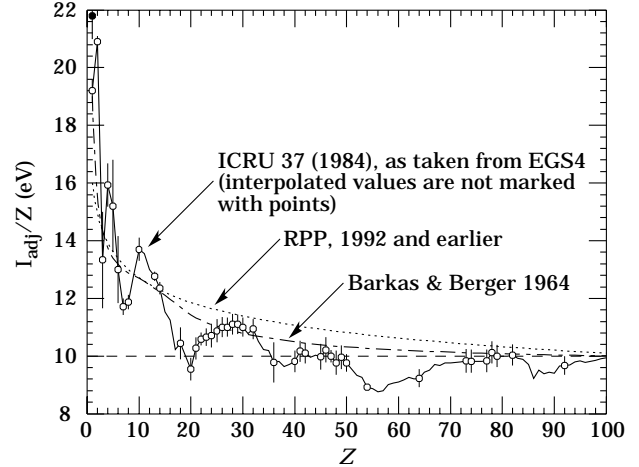


Figure 23.4: Excitation energies (divided by Z) as adopted by the ICRU [7]. Those based on measurement are shown by points with error flags; the interpolated values are simply joined. The solid point is for liquid H_2 ; the open point at 19.2 is for H_2 gas. Also shown are curves based on two approximate formulae.

23.2.1. The density effect: As the particle energy increases, its electric field flattens and extends, so that the distant-collision contribution to Eq. (23.1) increases as $\ln \beta\gamma$. However, real media become polarized, limiting the field extension and effectively truncating this part of the logarithmic rise [4,11–14]. At very high energies,

$$\delta/2 \rightarrow \ln(\hbar\omega_p/I) + \ln \beta\gamma - 1/2, \quad (23.3)$$

where $\delta/2$ is the density effect correction introduced in Eq. (23.1) and $\hbar\omega_p$ is the plasma energy defined in Table 23.1. A comparison with Eq. (23.1) shows that $|dE/dx|$ then grows as $\ln \beta\gamma$ rather than $\ln \beta^2 \gamma^2$, and that the mean excitation energy I is replaced by the plasma energy $\hbar\omega_p$. The stopping power as calculated with and without the density effect correction is shown in Fig. 23.1. Since the plasma frequency scales as the square root of the electron density, the correction is much larger for a liquid or solid than for a gas, as is illustrated by the examples in Fig. 23.2.

The density effect correction is usually computed using Sternheimer’s parameterization [11]:

$$\delta = \begin{cases} 2(\ln 10)x - \bar{C} & \text{if } x \geq x_1; \\ 2(\ln 10)x - \bar{C} + a(x_1 - x)^k & \text{if } x_0 \leq x < x_1; \\ 0 & \text{if } x < x_0 \text{ (nonconductors);} \\ \delta_0 10^{2(x-x_0)} & \text{if } x < x_0 \text{ (conductors)} \end{cases} \quad (23.4)$$

Here $x = \log_{10} \eta = \log_{10}(p/Mc)$. \bar{C} (the negative of the C used in Ref. 11) is obtained by equating the high-energy case of Eq. (23.4) to the limit given in Eq. (23.3). The other parameters are adjusted to give a best fit to the results of detailed calculations for momenta below $Mc \exp(x_1)$. Parameters for elements and nearly 200 compounds and mixtures of interest are published in a variety of places, notably in Ref. 14. A recipe for finding the coefficients for nontabulated materials given by Sternheimer and Peierls [13] is summarized in Ref. 10.

The remaining relativistic rise can be attributed to large energy transfers to a few electrons. If these escape or are otherwise accounted for separately, the energy deposited in an absorbing layer (in contrast to the energy lost by the particle) approaches a constant value, the Fermi plateau (see Sec. 23.2.5 below). The curve in Fig. 23.1 labeled “ $T_{\text{cut}} = 0.5 \text{ MeV}$ ” illustrates this behavior. At extreme energies (*e.g.*, $> 321 \text{ GeV}$ for muons in iron), radiative effects are more important than ionization losses. These are especially relevant for high-energy muons, as discussed in Sec. 23.6.

23.2.2. Energy loss at low energies: A shell correction C/Z is often included in the square brackets of Eq. (23.1) [3,5,7] to correct for atomic binding having been neglected in calculating some of the contributions to Eq. (23.1). We show the Barkas form [3] in Fig. 23.1. For copper it contributes about 1% at $\beta\gamma = 0.3$ (kinetic energy 6 MeV for a pion), and the correction decreases very rapidly with energy.

Eq. (23.1) is based on a first-order Born approximation. Higher-order corrections, again important only at lower energy, are normally included by adding a term $z^2 L_2(\beta)$ inside the square brackets.

An additional ‘‘Barkas correction’’ $zL_1(\beta)$ makes the stopping power for a negative particle somewhat larger than for a positive particle with the same mass and velocity. In a 1956 paper, Barkas *et al.* noted that negative pions had a longer range than positive pions [15]. The effect has been measured for a number of negative/positive particle pairs, most recently for antiprotons at the CERN LEAR facility [16].

A detailed discussion of low-energy corrections to the Bethe formula is given in ICRU Report 49 [5]. When the corrections are properly included, the accuracy of the Bethe-Bloch treatment is accurate to about 1% down to $\beta \approx 0.05$, or about 1 MeV for protons.

For $0.01 < \beta < 0.05$, there is no satisfactory theory. For protons, one usually relies on the empirical fitting formulae developed by Andersen and Ziegler [5,17]. For particles moving more slowly than $\approx 0.01c$ (more or less the velocity of the outer atomic electrons), Lindhard has been quite successful in describing electronic stopping power, which is proportional to β [18,19]. Finally, we note that at low energies, *e.g.*, for protons of less than several hundred eV, non-ionizing nuclear recoil energy loss dominates the total energy loss [5,19,20].

As shown in ICRU49 [5] (using data taken from Ref. 17), the nuclear plus electronic proton stopping power in copper is 113 MeV cm² g⁻¹ at $T = 10$ keV, rises to a maximum of 210 MeV cm² g⁻¹ at 100–150 keV, then falls to 120 MeV cm² g⁻¹ at 1 MeV. Above 0.5–1.0 MeV the corrected Bethe-Bloch theory is adequate.

23.2.3. Fluctuations in energy loss: The quantity $(dE/dx)\delta x$ is the mean energy loss via interaction with electrons in a layer of the medium with thickness δx . For finite δx , there are fluctuations in the actual energy loss. The distribution is skewed toward high values (the Landau tail) [1,21]. Only for a thick layer [$(dE/dx)\delta x \gg T_{\max}$] is the distribution nearly Gaussian. The large fluctuations in the energy loss are due to the small number of collisions involving large energy transfers. The fluctuations are smaller for the so-called restricted energy loss rate, as discussed in Sec. 23.2.5 below.

23.2.4. Energy loss in mixtures and compounds: A mixture or compound can be thought of as made up of thin layers of pure elements in the right proportion (Bragg additivity). In this case,

$$\frac{dE}{dx} = \sum w_j \left. \frac{dE}{dx} \right|_j, \quad (23.5)$$

where $dE/dx|_j$ is the mean rate of energy loss (in MeV g cm⁻²) in the j th element. Eq. (23.1) can be inserted into Eq. (23.5) to find expressions for $\langle Z/A \rangle$, $\langle I \rangle$, and $\langle \delta \rangle$; for example, $\langle Z/A \rangle = \sum w_j Z_j/A_j = \sum n_j Z_j / \sum n_j A_j$. However, $\langle I \rangle$ as defined this way is an underestimate, because in a compound electrons are more tightly bound than in the free elements, and $\langle \delta \rangle$ as calculated this way has little relevance, because it is the electron density which matters. If possible, one uses the tables given in Refs. 14 and 10, which include effective excitation energies and interpolation coefficients for calculating the density effect correction for the chemical elements and nearly 200 mixtures and compounds. If a compound or mixture is not found, then one uses the recipe for δ given in Ref. 13 (or Ref. 22), and calculates $\langle I \rangle$ according to the discussion in Ref. 9. (Note the ‘‘13% rule!’’)

23.2.5. Restricted energy loss rates for relativistic ionizing particles: Fluctuations in energy loss are due mainly to the production of a few high-energy knock-on electrons. Practical detectors often measure the energy *deposited*, not the energy *lost*. When energy is carried off by energetic knock-on electrons, it is more appropriate to consider the mean energy loss excluding energy transfers greater than

some cutoff T_{cut} . The restricted energy loss rate is

$$-\left. \frac{dE}{dx} \right|_{T < T_{\text{cut}}} = K z^2 \frac{Z}{A} \frac{1}{\beta^2} \left[\frac{1}{2} \ln \frac{2m_e c^2 \beta^2 \gamma^2 T_{\text{upper}}}{I^2} - \frac{\beta^2}{2} \left(1 + \frac{T_{\text{upper}}}{T_{\text{max}}} \right) - \frac{\delta}{2} \right] \quad (23.6)$$

where $T_{\text{upper}} = \text{MIN}(T_{\text{cut}}, T_{\text{max}})$. This form agrees with the equation given in previous editions of this *Review* [23] for $T_{\text{cut}} \ll T_{\text{max}}$ but smoothly joins the normal Bethe-Bloch function (Eq. (23.1)) for $T_{\text{cut}} > T_{\text{max}}$.

23.2.6. Energetic knock-on electrons (δ rays): The distribution of secondary electrons with kinetic energies $T \gg I$ is given by [1]

$$\frac{d^2 N}{dT dx} = \frac{1}{2} K z^2 \frac{Z}{A} \frac{1}{\beta^2} \frac{F(T)}{T^2} \quad (23.7)$$

for $I \ll T \leq T_{\text{max}}$, where T_{max} is given by Eq. (23.2). The factor F is spin-dependent, but is about unity for $T \ll T_{\text{max}}$. For spin-0 particles $F(T) = (1 - \beta^2 T/T_{\text{max}})$; forms for spins 1/2 and 1 are also given by Rossi [1]. When Eq. (23.7) is integrated from T_{cut} to T_{max} , one obtains the difference between Eq. (23.1) and Eq. (23.6). For incident electrons, the indistinguishability of projectile and target means that the range of T extends only to half the kinetic energy of the incident particle. Additional formulae are given in Ref. 24. Equation (23.7) is inaccurate for T close to I : for $2I \lesssim T \lesssim 10I$, the $1/T^2$ dependence above becomes approximately $T^{-\eta}$, with $3 \lesssim \eta \lesssim 5$ [25].

23.2.7. Ionization yields: Physicists frequently relate total energy loss to the number of ion pairs produced near the particle’s track. This relation becomes complicated for relativistic particles due to the wandering of energetic knock-on electrons whose ranges exceed the dimensions of the fiducial volume. For a qualitative appraisal of the nonlocality of energy deposition in various media by such modestly energetic knock-on electrons, see Ref. 26. The mean local energy dissipation per local ion pair produced, W , while essentially constant for relativistic particles, increases at slow particle speeds [27]. For gases, W can be surprisingly sensitive to trace amounts of various contaminants [27]. Furthermore, ionization yields in practical cases may be greatly influenced by such factors as subsequent recombination [28].

23.3. Multiple scattering through small angles

A charged particle traversing a medium is deflected by many small-angle scatters. Most of this deflection is due to Coulomb scattering from nuclei, and hence the effect is called multiple Coulomb scattering. (However, for hadronic projectiles, the strong interactions also contribute to multiple scattering.) The Coulomb scattering distribution is well represented by the theory of Molière [29]. It is roughly Gaussian for small deflection angles, but at larger angles (greater than a few θ_0 , defined below) it behaves like Rutherford scattering, having larger tails than does a Gaussian distribution.

If we define

$$\theta_0 = \theta_{\text{plane}}^{\text{rms}} = \frac{1}{\sqrt{2}} \theta_{\text{space}}^{\text{rms}}. \quad (23.8)$$

then it is sufficient for many applications to use a Gaussian approximation for the central 98% of the projected angular distribution, with a width given by [30,31]

$$\theta_0 = \frac{13.6 \text{ MeV}}{\beta c p} z \sqrt{x/X_0} \left[1 + 0.038 \ln(x/X_0) \right]. \quad (23.9)$$

Here p , βc , and z are the momentum, velocity, and charge number of the incident particle, and x/X_0 is the thickness of the scattering medium in radiation lengths (defined below). This value of θ_0 is from a fit to Molière distribution [29] for singly charged particles with $\beta = 1$ for all Z , and is accurate to 11% or better for $10^{-3} < x/X_0 < 100$.

Eq. (23.9) describes scattering from a single material, while the usual problem involves the multiple scattering of a particle traversing many different layers and mixtures. Since it is from a fit to a Molière distribution, it is incorrect to add the individual θ_0 contributions in quadrature; the result is systematically too small. It is much more accurate to apply Eq. (23.9) once, after finding x and X_0 for the combined scatterer.

Lynch and Dahl have extended this phenomenological approach, fitting Gaussian distributions to a variable fraction of the Molière distribution for arbitrary scatterers [31], and achieve accuracies of 2% or better.

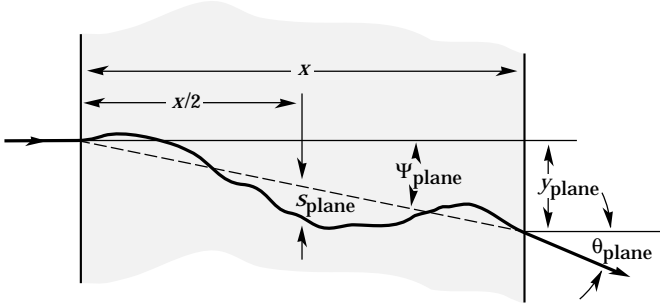


Figure 23.5: Quantities used to describe multiple Coulomb scattering. The particle is incident in the plane of the figure.

The nonprojected (space) and projected (plane) angular distributions are given approximately by [29]

$$\frac{1}{2\pi\theta_0^2} \exp\left(-\frac{\theta_{\text{space}}^2}{2\theta_0^2}\right) d\Omega, \quad (23.10)$$

$$\frac{1}{\sqrt{2\pi}\theta_0} \exp\left(-\frac{\theta_{\text{plane}}^2}{2\theta_0^2}\right) d\theta_{\text{plane}}, \quad (23.11)$$

where θ is the deflection angle. In this approximation, $\theta_{\text{space}}^2 \approx (\theta_{\text{plane},x}^2 + \theta_{\text{plane},y}^2)$, where the x and y axes are orthogonal to the direction of motion, and $d\Omega \approx d\theta_{\text{plane},x} d\theta_{\text{plane},y}$. Deflections in $\theta_{\text{plane},x}$ and $\theta_{\text{plane},y}$ are independent and identically distributed.

Figure 23.5 shows these and other quantities sometimes used to describe multiple Coulomb scattering. They are

$$\psi_{\text{plane}}^{\text{rms}} = \frac{1}{\sqrt{3}} \theta_{\text{plane}}^{\text{rms}} = \frac{1}{\sqrt{3}} \theta_0, \quad (23.12)$$

$$y_{\text{plane}}^{\text{rms}} = \frac{1}{\sqrt{3}} x \theta_{\text{plane}}^{\text{rms}} = \frac{1}{\sqrt{3}} x \theta_0, \quad (23.13)$$

$$s_{\text{plane}}^{\text{rms}} = \frac{1}{4\sqrt{3}} x \theta_{\text{plane}}^{\text{rms}} = \frac{1}{4\sqrt{3}} x \theta_0. \quad (23.14)$$

All the quantitative estimates in this section apply only in the limit of small $\theta_{\text{plane}}^{\text{rms}}$ and in the absence of large-angle scatters. The random variables s , ψ , y , and θ in a given plane are distributed in a correlated fashion (see Sec. 28.1 of this *Review* for the definition of the correlation coefficient). Obviously, $y \approx x\psi$. In addition, y and θ have the correlation coefficient $\rho_{y\theta} = \sqrt{3}/2 \approx 0.87$. For Monte Carlo generation of a joint $(y_{\text{plane}}, \theta_{\text{plane}})$ distribution, or for other calculations, it may be most convenient to work with independent Gaussian random variables (z_1, z_2) with mean zero and variance one, and then set

$$y_{\text{plane}} = z_1 x \theta_0 (1 - \rho_{y\theta}^2)^{1/2} / \sqrt{3} + z_2 \rho_{y\theta} x \theta_0 / \sqrt{3} \\ = z_1 x \theta_0 / \sqrt{12} + z_2 x \theta_0 / 2; \quad (23.15)$$

$$\theta_{\text{plane}} = z_2 \theta_0. \quad (23.16)$$

Note that the second term for y_{plane} equals $x \theta_{\text{plane}}/2$ and represents the displacement that would have occurred had the deflection θ_{plane} all occurred at the single point $x/2$.

For heavy ions the multiple Coulomb scattering has been measured and compared with various theoretical distributions [32].

23.4. Radiation length and associated quantities

In dealing with electrons and photons at high energies, it is convenient to measure the thickness of the material in units of the radiation length X_0 . This is the mean distance over which a high-energy electron loses all but $1/e$ of its energy by bremsstrahlung, and is the appropriate scale length for describing high-energy electromagnetic cascades. X_0 has been calculated and tabulated by Y.S. Tsai [33]:

$$\frac{1}{X_0} = 4\alpha r_e^2 \frac{N_A}{A} \left\{ Z^2 [L_{\text{rad}} - f(Z)] + Z L'_{\text{rad}} \right\}. \quad (23.17)$$

For $A = 1 \text{ g mol}^{-1}$, $4\alpha r_e^2 N_A/A = (716.408 \text{ g cm}^{-2})^{-1}$. L_{rad} and L'_{rad} are given in Table 23.2. The function $f(Z)$ is an infinite sum, but for elements up to uranium can be represented to 4-place accuracy by

$$f(Z) = a^2 [(1 + a^2)^{-1} + 0.20206 \\ - 0.0369 a^2 + 0.0083 a^4 - 0.002 a^6], \quad (23.18)$$

where $a = \alpha Z$ [34].

Table 23.2: Tsai's L_{rad} and L'_{rad} , for use in calculating the radiation length in an element using Eq. (23.17).

Element	Z	L_{rad}	L'_{rad}
H	1	5.31	6.144
He	2	4.79	5.621
Li	3	4.74	5.805
Be	4	4.71	5.924
Others	> 4	$\ln(184.15 Z^{-1/3})$	$\ln(1194 Z^{-2/3})$

Although it is easy to use Eq. (23.17) to calculate X_0 , the functional dependence on Z is somewhat hidden. Dahl provides a compact fit to the data [35]:

$$X_0 = \frac{716.4 \text{ g cm}^{-2} A}{Z(Z+1) \ln(287/\sqrt{Z})} \quad (23.19)$$

Results obtained with this formula agree with Tsai's values to better than 2.5% for all elements except helium, where the result is about 5% low.

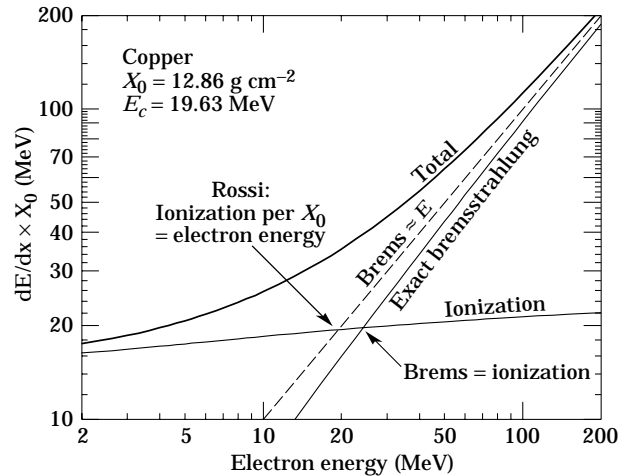


Figure 23.6: Two definitions of the critical energy E_c .

The radiation length in a mixture or compound may be approximated by

$$1/X_0 = \sum w_j / X_j, \quad (23.20)$$

where w_j and X_j are the fraction by weight and the radiation length for the j th element.

An electron loses energy by bremsstrahlung at a rate nearly proportional to its energy, while the ionization loss rate varies only logarithmically with the electron energy. The *critical energy* E_c is sometimes defined as the energy at which the two loss rates are equal [36]. Berger and Seltzer [36] also give the approximation $E_c = (800 \text{ MeV})/(Z + 1.2)$. This formula has been widely quoted, and has been given in previous editions of this *Review* [23]. Among alternate definitions is that of Rossi [1], who defines the critical energy as the energy at which the ionization loss per radiation length is equal to the electron energy. Equivalently, it is the same as the first definition with the approximation $|dE/dx|_{\text{brems}} \approx E/X_0$. These definitions are illustrated in the case of copper in Fig. 23.6.

The accuracy of approximate forms for E_c has been limited by the failure to distinguish between gases and solid or liquids, where there

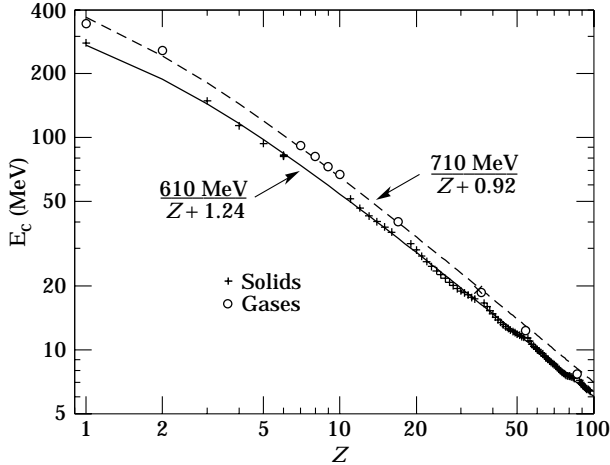


Figure 23.7: Electron critical energy for the chemical elements, using Rossi’s definition [1]. The fits shown are for solids and liquids (solid line) and gases (dashed line). The rms deviation is 2.2% for the solids and 4.0% for the gases. (Computed with code supplied by A. Fassó.)

is a substantial difference in ionization at the relevant energy because of the density effect. We distinguish these two cases in Fig. 23.7. Fits were also made with functions of the form $a/(Z+b)^\alpha$, but α was essentially unity.

The transverse development of electromagnetic showers in different materials scales fairly accurately with the *Molière radius* R_M , given by [37,38]

$$R_M = X_0 E_s/E_c, \quad (23.21)$$

where $E_s \approx 21$ MeV (see Table 23.1), and the Rossi definition of E_c is used.

In a material containing a weight fraction w_j of the element with critical energy E_{cj} and radiation length X_j , the Molière radius is given by

$$\frac{1}{R_M} = \frac{1}{E_s} \sum \frac{w_j E_{cj}}{X_j}. \quad (23.22)$$

For very high-energy photons, the total e^+e^- pair-production cross section is approximately

$$\sigma = \frac{7}{9}(A/X_0 N_A), \quad (23.23)$$

where A is the atomic weight of the material and N_A is Avogadro’s number. Equation Eq. (23.23) is accurate to within a few percent down to energies as low as 1 GeV. The cross section decreases at lower energies, as shown in Fig. 24.4 of this *Review*. As the energy decreases, a number of other processes become important, as is shown in Fig. 24.3 of this *Review*.

23.5. Electromagnetic cascades

When a high-energy electron or photon is incident on a thick absorber, it initiates an electromagnetic cascade as pair production and bremsstrahlung generate more electrons and photons with lower energy. The longitudinal development is governed by the high-energy part of the cascade, and therefore scales as the radiation length in the material. Electron energies eventually fall below the critical energy, and then dissipate their energy by ionization and excitation rather than by the generation of more shower particles. In describing shower behavior, it is therefore convenient to introduce the scale variables

$$\begin{aligned} t &= x/X_0 \\ y &= E/E_c, \end{aligned} \quad (23.24)$$

so that distance is measured in units of radiation length and energy in units of critical energy.

Longitudinal profiles for an EGS4 [22] simulation of a 30 GeV electron-induced cascade in iron are shown in Fig. 23.8. The number of particles crossing a plane (very close to Rossi’s Π function [1]) is sensitive to the cutoff energy, here chosen as a total energy of

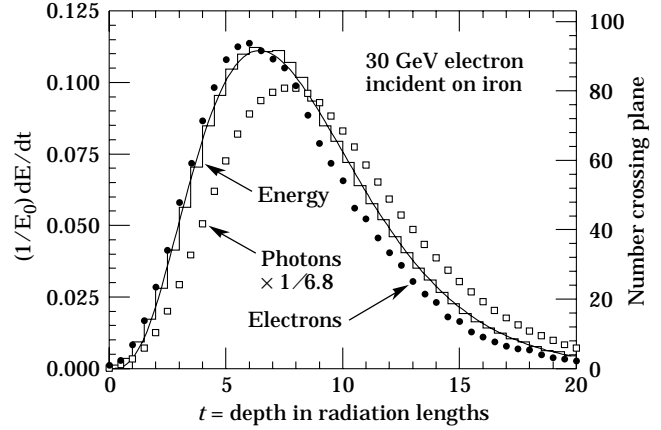


Figure 23.8: An EGS4 simulation of a 30 GeV electron-induced cascade in iron. The histogram shows fractional energy deposition per radiation length, and the curve is a gamma-function fit to the distribution. Circles indicate the number of electrons with total energy greater than 1.5 MeV crossing planes at $X_0/2$ intervals (scale on right) and the squares the number of photons with $E \geq 1.5$ MeV crossing the planes (scaled down to have same area as the electron distribution).

1.5 MeV for both electrons and photons. The electron number falls off more quickly than energy deposition. This is because, with increasing depth, a larger fraction of the cascade energy is carried by photons. Exactly what a calorimeter measures depends on the device, but it is not likely to be exactly any of the profiles shown. In gas counters it may be very close to the electron number, but in glass Čerenkov detectors and other devices with “thick” sensitive regions it is closer to the energy deposition (total track length). In such detectors the signal is proportional to the “detectable” track length T_d , which is in general less than the total track length T . Practical devices are sensitive to electrons with energy above some detection threshold E_d , and $T_d = T F(E_d/E_c)$. An analytic form for $F(E_d/E_c)$ obtained by Rossi [1] is given by Fabjan [39]; see also Amaldi [40].

The mean longitudinal profile of the energy deposition in an electromagnetic cascade is reasonably well described by a gamma distribution [41]:

$$\frac{dE}{dt} = E_0 b \frac{(bt)^{a-1} e^{-bt}}{\Gamma(a)} \quad (23.25)$$

The maximum t_{\max} occurs at $(a-1)/b$. We have made fits to shower profiles in elements ranging from carbon to uranium, at energies from 1 GeV to 100 GeV. The energy deposition profiles are well described by Eq. (23.25) with

$$t_{\max} = (a-1)/b = 1.0 \times (\ln y + C_j), \quad j = e, \gamma, \quad (23.26)$$

where $C_e = -0.5$ for electron-induced cascades and $C_\gamma = +0.5$ for photon-induced cascades. To use Eq. (23.25), one finds $(a-1)/b$ from Eq. (23.26) and Eq. (23.24), then finds a either by assuming $b \approx 0.5$ or by finding a more accurate value from Fig. 23.9. The results are very similar for the electron number profiles, but there is some dependence on the atomic number of the medium. A similar form for the electron number maximum was obtained by Rossi in the context of his “Approximation B,” [1] (see Fabjan’s review in Ref. 39), but with $C_e = -1.0$ and $C_\gamma = -0.5$; we regard this as superseded by the EGS4 result.

The “shower length” $X_s = X_0/b$ is less conveniently parameterized, since b depends upon both Z and incident energy, as shown in Fig. 23.9. As a corollary of this Z dependence, the number of electrons crossing a plane near shower maximum is underestimated using Rossi’s approximation for carbon and seriously overestimated for uranium. Essentially the same b values are obtained for incident electrons and photons. For many purposes it is sufficient to take $b \approx 0.5$.

The gamma distribution is very flat near the origin, while the EGS4 cascade (or a real cascade) increases more rapidly. As a result Eq. (23.25) fails badly for about the first two radiation lengths; it was necessary to exclude this region in making fits.

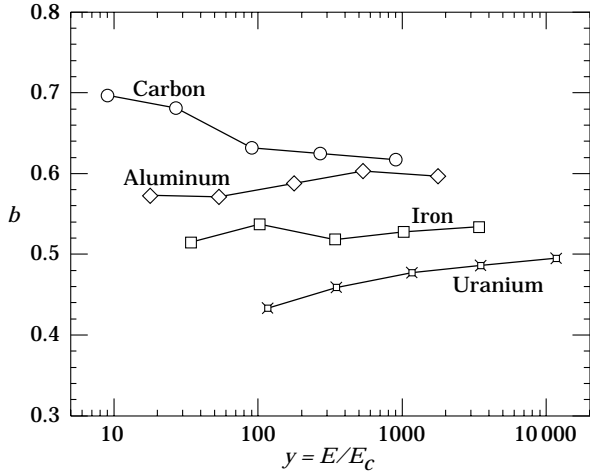


Figure 23.9: Fitted values of the scale factor b for energy deposition profiles obtained with EGS4 for a variety of elements for incident electrons with $1 \leq E_0 \leq 100$ GeV. Values obtained for incident photons are essentially the same.

Because fluctuations are important, Eq. (23.25) should be used only in applications where average behavior is adequate. Grindhammer *et al.* have developed fast simulation algorithms in which the variance and correlation of a and b are obtained by fitting Eq. (23.25) to individually simulated cascades, then generating profiles for cascades using a and b chosen from the correlated distributions [42].

Measurements of the lateral distribution in electromagnetic cascades are shown in Refs. 37 and 38. On the average, only 10% of the energy lies outside the cylinder with radius R_M . About 99% is contained inside of $3.5R_M$, but at this radius and beyond composition effects become important and the scaling with R_M fails. The distributions are characterized by a narrow core, and broaden as the shower develops. They are often represented as the sum of two Gaussians, and Grindhammer [42] describes them with the function

$$f(r) = \frac{2r R^2}{(r^2 + R^2)^2}, \quad (23.27)$$

where R is a phenomenological function of x/X_0 and $\ln E$.

23.6. Muon energy loss at high energy

At sufficiently high energies, radiative processes become more important than ionization for all charged particles. For muons and pions in materials such as iron, this “critical energy” occurs at several hundred GeV. Radiative effects dominate the energy loss of energetic muons found in cosmic rays or produced at the newest accelerators. These processes are characterized by small cross sections, hard spectra, large energy fluctuations, and the associated generation of electromagnetic and (in the case of photonuclear interactions) hadronic showers [45–53]. As a consequence, at these energies the treatment of energy loss as a uniform and continuous process is for many purposes inadequate.

It is convenient to write the average rate of muon energy loss as [43]

$$-dE/dx = a(E) + b(E)E. \quad (23.28)$$

Here $a(E)$ is the ionization energy loss given by Eq. (23.1), and $b(E)$ is the sum of e^+e^- pair production, bremsstrahlung, and photonuclear contributions. To the approximation that these slowly-varying functions are constant, the mean range x_0 of a muon with initial energy E_0 is given by

$$x_0 \approx (1/b) \ln(1 + E_0/E_{\mu c}), \quad (23.29)$$

where $E_{\mu c} = a/b$. Figure 23.10 shows contributions to $b(E)$ for iron. Since $a(E) \approx 0.002$ GeV g⁻¹ cm², $b(E)E$ dominates the energy loss above several hundred GeV, where $b(E)$ is nearly constant. The rate of energy loss for muons in hydrogen, uranium, and iron is shown in Fig. 23.11 [44].

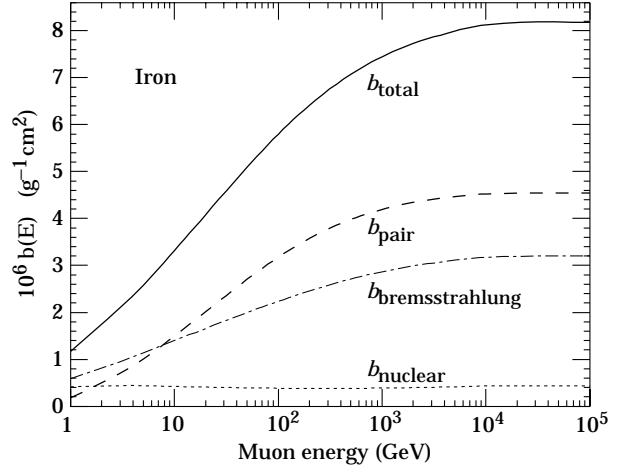


Figure 23.10: Contributions to the fractional energy loss by muons in iron due to e^+e^- pair production, bremsstrahlung, and photonuclear interactions, as obtained from Lohmann *et al.* [44].

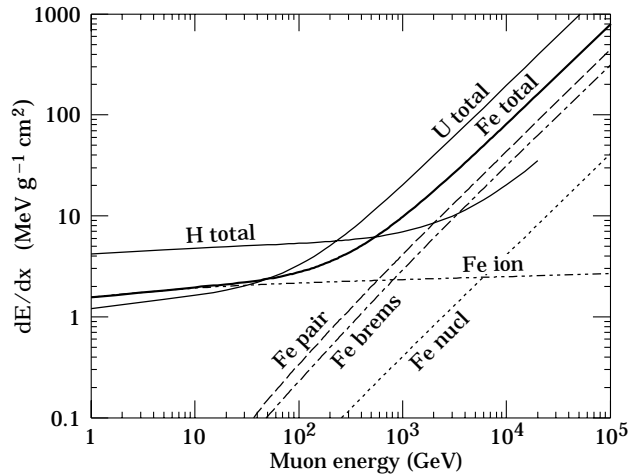


Figure 23.11: The average energy loss of a muon in hydrogen, iron, and uranium as a function of muon energy. Contributions to dE/dx in iron from ionization and the processes shown in Fig. 23.10 are also shown.

The “muon critical energy” $E_{\mu c}$ can be defined more exactly as the energy at which radiative and ionization losses are equal, and can be found by solving $E_{\mu c} = a(E_{\mu c})/b(E_{\mu c})$. This definition corresponds to the solid-line intersection in Fig. 23.6, and is different from the Rossi definition we used for electrons. It serves the same function: below $E_{\mu c}$ ionization losses dominate, and above $E_{\mu c}$ radiative losses dominate. The dependence of $E_{\mu c}$ on atomic number Z is shown in Fig. 23.12.

The radiative cross sections are expressed as functions of the fractional energy loss ν . The bremsstrahlung cross section goes roughly as $1/\nu$ over most of the range, while for the pair production case the distribution goes as ν^{-3} to ν^{-2} (see Ref. 55). “Hard” losses are therefore more probable in bremsstrahlung, and in fact energy losses due to pair production may very nearly be treated as continuous. The calculated momentum distribution of an incident 1 TeV/ c muon beam after it crosses 3 m of iron is shown in Fig. 23.13. The most probable loss is 9 GeV, or 3.8 MeV g⁻¹ cm². The full width at half maximum is 7 GeV/ c , or 0.7%. The radiative tail is almost entirely due to bremsstrahlung; this includes most of the 10% that lost more than 2.8% of their energy. Most of the 3.3% that lost more than 10% of their incident energy experienced photonuclear interactions, which are concentrated in rare, relatively hard collisions. The latter can exceed nominal detector resolution [56], necessitating the reconstruction of lost energy. Electromagnetic and hadronic cascades in detector materials can obscure muon tracks in detector planes and reduce tracking efficiency [57].

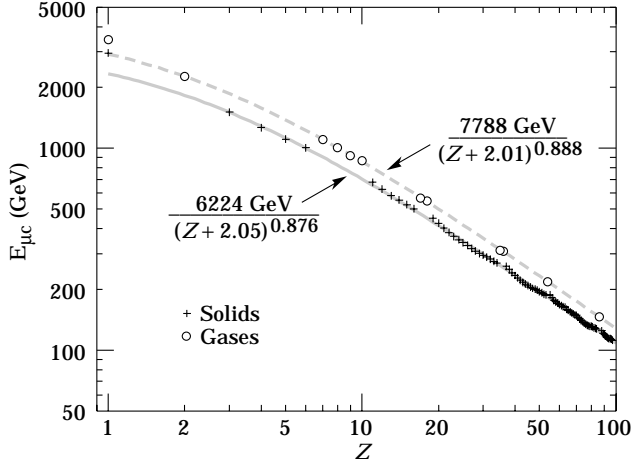


Figure 23.12: Muon critical energy for the chemical elements, defined as the energy at which radiative and ionization energy loss rates are equal. The equality comes at a higher energy for gases than for solids or liquids with the same atomic number because of a smaller density effect reduction of the ionization losses. The fits shown in the figure exclude hydrogen. Alkali metals fall 3–4% above the fitted function, while most other solids are within 2% of the function. Among the gases the worst fit is for neon (1.4% high). (Courtesy of N.V. Mokhov and S.I. Striganov.)

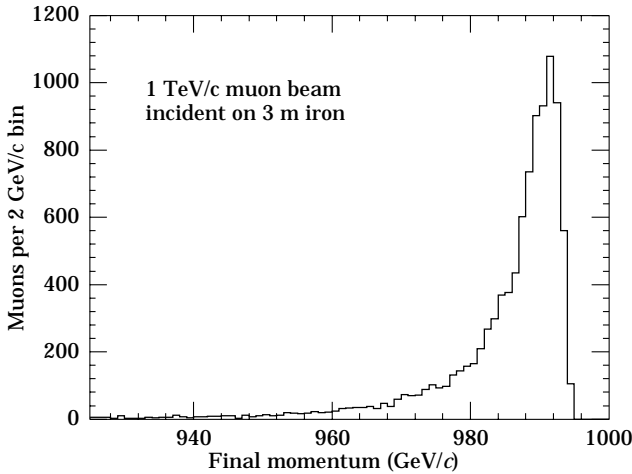


Figure 23.13: The momentum distribution of 1 TeV/c muons after traversing 3 m of iron, as obtained with Van Ginniken’s TRAMU muon transport code [55].

23.7. Čerenkov and transition radiation [4,58,59]

A charged particle radiates if its velocity is greater than the local phase velocity of light (Čerenkov radiation) or if it crosses suddenly from one medium to another with different optical properties (transition radiation). Neither process is important for energy loss, but both are used in high-energy physics detectors.

Čerenkov Radiation. The half-angle θ_c of the Čerenkov cone for a particle with velocity βc in a medium with index of refraction n is

$$\theta_c = \arccos(1/n\beta) \approx \sqrt{2(1-1/n\beta)} \quad \text{for small } \theta_c, \text{ e.g. in gases.} \quad (23.30)$$

The threshold velocity β_t is $1/n$, and $\gamma_t = 1/(1-\beta_t^2)^{1/2}$. Therefore, $\beta_t \gamma_t = 1/(2\delta + \delta^2)^{1/2}$, where $\delta = n - 1$. Values of δ for various commonly used gases are given as a function of pressure and wavelength in Ref. 60. For values at atmospheric pressure, see Table 6.1. Data for other commonly used materials are given in Ref. 61.

The number of photons produced per unit path length of a particle with charge ze and per unit energy interval of the photons is

$$\frac{d^2 N}{dE dx} = \frac{\alpha z^2}{\hbar c} \sin^2 \theta_c = \frac{\alpha^2 z^2}{r_e m_e c^2} \left(1 - \frac{1}{\beta^2 n^2(E)}\right) \approx 370 \sin^2 \theta_c(E) \text{ eV}^{-1} \text{ cm}^{-1} \quad (z = 1), \quad (23.31)$$

or, equivalently,

$$\frac{d^2 N}{dx d\lambda} = \frac{2\pi\alpha z^2}{\lambda^2} \left(1 - \frac{1}{\beta^2 n^2(\lambda)}\right). \quad (23.32)$$

The index of refraction is a function of photon energy E , as is the sensitivity of the transducer used to detect the light. For practical use, Eq. (23.31) must be multiplied by the the transducer response function and integrated over the region for which $\beta n(E) > 1$. Further details are given in the discussion of Čerenkov detectors in the Detectors section (Sec. 25 of this Review).

Transition Radiation. The energy radiated when a particle with charge ze crosses the boundary between vacuum and a medium with plasma frequency ω_p is

$$I = \alpha z^2 \gamma \hbar \omega_p / 3, \quad (23.33)$$

where

$$\begin{aligned} \hbar \omega_p &= \sqrt{4\pi N_e r_e^3} m_e c^2 / \alpha \\ &= \sqrt{4\pi N_e a_\infty^3} 2 \times 13.6 \text{ eV}. \end{aligned} \quad (23.34)$$

Here N_e is the electron density in the medium, r_e is the classical electron radius, and a_∞ is the Bohr radius. For styrene and similar materials, $\sqrt{4\pi N_e a_\infty^3} \approx 0.8$, so that $\hbar \omega_p \approx 20$ eV. The typical emission angle is $1/\gamma$.

The radiation spectrum is logarithmically divergent at low energies and decreases rapidly for $\hbar\omega/\gamma\hbar\omega_p > 1$. About half the energy is emitted in the range $0.1 \leq \hbar\omega/\gamma\hbar\omega_p \leq 1$. For a particle with $\gamma = 10^3$, the radiated photons are in the soft x-ray range 2 to 20 eV. The γ dependence of the emitted energy thus comes from the hardening of the spectrum rather than from an increased quantum yield. For a typical radiated photon energy of $\gamma\hbar\omega_p/4$, the quantum yield is

$$\begin{aligned} N_\gamma &\approx \frac{1}{2} \frac{\alpha z^2 \gamma \hbar \omega_p}{3} / \frac{\gamma \hbar \omega_p}{4} \\ &\approx \frac{2}{3} \alpha z^2 \approx 0.5\% \times z^2. \end{aligned} \quad (23.35)$$

More precisely, the number of photons with energy $\hbar\omega > \hbar\omega_0$ is given by [4]

$$N_\gamma(\hbar\omega > \hbar\omega_0) = \frac{\alpha z^2}{\pi} \left[\left(\ln \frac{\gamma \hbar \omega_p}{\hbar \omega_0} - 1 \right)^2 + \frac{\pi^2}{12} \right], \quad (23.36)$$

within corrections of order $(\hbar\omega_0/\gamma\hbar\omega_p)^2$. The number of photons above a fixed energy $\hbar\omega_0 \ll \gamma\hbar\omega_p$ thus grows as $(\ln \gamma)^2$, but the number above a fixed fraction of $\gamma\hbar\omega_p$ (as in the example above) is constant. For example, for $\hbar\omega > \gamma\hbar\omega_p/10$, $N_\gamma = 2.519 \alpha z^2 / \pi = 0.59\% \times z^2$.

The yield can be increased by using a stack of plastic foils with gaps between. However, interference can be important, and the soft x rays are readily absorbed in the foils. The first problem can be overcome by choosing thicknesses and spacings large compared to the “formation length” $D = \gamma c / \omega_p$, which in practical situations is tens of μm . Other practical problems are discussed in Sec. 25.

References:

1. B. Rossi, *High Energy Particles*, Prentice-Hall, Inc., Englewood Cliffs, NJ, 1952.
2. U. Fano, *Ann. Rev. Nucl. Sci.* **13**, 1 (1963).
3. W.H. Barkas and M.J. Berger, *Tables of Energy Losses and Ranges of Heavy Charged Particles*, NASA-SP-3013 (1964).
4. J.D. Jackson, *Classical Electrodynamics*, 3rd edition, (John Wiley & Sons, New York, 1998).
5. “Stopping Powers and Ranges for Protons and Alpha Particles,” ICRU Report No. 49 (1993).
6. J.D. Jackson, “Effect of Form Factor on dE/dx from Close Collisions,” Particle Data Group Note PDG-93-04 (19 October 1993) (unpublished).

7. "Stopping Powers for Electrons and Positrons," ICRU Report No. 37 (1984).
8. <http://physics.nist.gov/PhysRefData/XrayMassCoef/tab1.html>.
9. S.M. Seltzer and M.J. Berger, *Int. J. of Applied Rad.* **33**, 1189 (1982).
10. S.M. Seltzer and M.J. Berger, *Int. J. of Applied Rad.* **35**, 665 (1984). This paper corrects and extends the results of Ref. 9.
11. R.M. Sternheimer, *Phys. Rev.* **88**, 851 (1952).
12. A. Crispin and G.N. Fowler, *Rev. Mod. Phys.* **42**, 290 (1970).
13. R.M. Sternheimer and R.F. Peierls, *Phys. Rev.* **B3**, 3681 (1971).
14. R.M. Sternheimer, S.M. Seltzer, and M.J. Berger, "The Density Effect for the Ionization Loss of Charged Particles in Various Substances," *Atomic Data & Nucl. Data Tables* **30**, 261 (1984). An error resulting from an incorrect chemical formula for lanthanum oxysulfide is corrected in a footnote in Ref. 10. Chemical composition for the tabulated materials is given in Ref. 9.
15. W.H. Barkas, W. Birnbaum, and F.M. Smith, *Phys. Rev.* **101**, 778 (1956).
16. M. Agnello *et al.*, *Phys. Rev. Lett.* **74**, 371 (1995).
17. H.H. Andersen and J.F. Ziegler, *Hydrogen: Stopping Powers and Ranges in All Elements*. Vol. 3 of *The Stopping and Ranges of Ions in Matter* (Pergamon Press 1977).
18. J. Lindhard, *Kgl. Danske Videnskab. Selskab, Mat.-Fys. Medd.* **28**, No. 8 (1954).
19. J. Lindhard, M. Scharff, and H.E. Schiøtt, *Kgl. Danske Videnskab. Selskab, Mat.-Fys. Medd.* **33**, No. 14 (1963).
20. J.F. Ziegler, J.F. Biersac, and U. Littmark, *The Stopping and Range of Ions in Solids*, Pergamon Press 1985.
21. L.D. Landau, *J. Exp. Phys. (USSR)* **8**, 201 (1944); See, for instance, K.A. Ispirian, A.T. Margarian, and A.M. Zverev, *Nucl. Instrum. Methods* **117**, 125 (1974).
22. W.R. Nelson, H. Hirayama, and D.W.O. Rogers, "The EGS4 Code System," SLAC-265, Stanford Linear Accelerator Center (Dec. 1985).
23. K. Hikasa *et al.*, *Review of Particle Properties*, *Phys. Rev.* **D46** (1992) S1.
24. For unit-charge projectiles, see E.A. Uehling, *Ann. Rev. Nucl. Sci.* **4**, 315 (1954). For highly charged projectiles, see J.A. Doggett and L.V. Spencer, *Phys. Rev.* **103**, 1597 (1956). A Lorentz transformation is needed to convert these center-of-mass data to knock-on energy spectra.
25. N.F. Mott and H.S.W. Massey, *The Theory of Atomic Collisions*, Oxford Press, London, 1965.
26. L.V. Spencer "Energy Dissipation by Fast Electrons," Nat'l Bureau of Standards Monograph No. 1 (1959).
27. "Average Energy Required to Produce an Ion Pair," ICRU Report No. 31 (1979).
28. N. Hadley *et al.*, "List of Poisoning Times for Materials," Lawrence Berkeley Lab Report TPC-LBL-79-8 (1981).
29. H.A. Bethe, *Phys. Rev.* **89**, 1256 (1953). A thorough review of multiple scattering is given by W.T. Scott, *Rev. Mod. Phys.* **35**, 231 (1963). However, the data of Shen *et al.*, (*Phys. Rev.* **D20**, 1584 (1979)) show that Bethe's simpler method of including atomic electron effects agrees better with experiment than does Scott's treatment. For a thorough discussion of simple formulae for single scatters and methods of compounding these into multiple-scattering formulae, see W.T. Scott, *Rev. Mod. Phys.* **35**, 231 (1963). For detailed summaries of formulae for computing single scatters, see J.W. Motz, H. Olsen, and H.W. Koch, *Rev. Mod. Phys.* **36**, 881 (1964).
30. V.L. Highland, *Nucl. Instrum. Methods* **129**, 497 (1975), and *Nucl. Instrum. Methods* **161**, 171 (1979).
31. G.R. Lynch and O.I. Dahl, *Nucl. Instrum. Methods* **B58**, 6 (1991).
32. M. Wong *et al.*, *Med. Phys.* **17**, 163 (1990).
33. Y.S. Tsai, *Rev. Mod. Phys.* **46**, 815 (1974).
34. H. Davies, H.A. Bethe, and L.C. Maximon, *Phys. Rev.* **93**, 788 (1954).
35. O.I. Dahl, private communication.
36. M.J. Berger and S.M. Seltzer, "Tables of Energy Losses and Ranges of Electrons and Positrons," National Aeronautics and Space Administration Report NASA-SP-3012 (Washington DC 1964).
37. W.R. Nelson, T.M. Jenkins, R.C. McCall, and J.K. Cobb, *Phys. Rev.* **149**, 201 (1966).
38. G. Bathow *et al.*, *Nucl. Phys.* **B20**, 592 (1970).
39. *Experimental Techniques in High Energy Physics*, ed. by T. Ferbel (Addison-Wesley, Menlo Park CA 1987).
40. U. Amaldi, *Phys. Scripta* **23**, 409 (1981).
41. E. Longo and I. Sestili, *Nucl. Instrum. Methods* **128**, 283 (1975).
42. G. Grindhammer *et al.*, in *Proceedings of the Workshop on Calorimetry for the Supercollider*, Tuscaloosa, AL, March 13–17, 1989, edited by R. Donaldson and M.G.D. Gilchriese (World Scientific, Teaneck, NJ, 1989), p. 151.
43. P.H. Barrett, L.M. Bollinger, G. Cocconi, Y. Eisenberg, and K. Greisen, *Rev. Mod. Phys.* **24**, 133 (1952).
44. W. Lohmann, R. Kopp, and R. Voss, "Energy Loss of Muons in the Energy Range 1–10000 GeV," CERN Report 85–03 (1985).
45. H.A. Bethe and W. Heitler, *Proc. Roy. Soc.* **A146**, 83 (1934); H.A. Bethe, *Proc. Cambridge Phil. Soc.* **30**, 542 (1934).
46. A.A. Petrukhin and V.V. Shestakov, *Can. J. Phys.* **46**, S377 (1968).
47. V.M. Galitskii and S.R. Kel'ner, *Sov. Phys. JETP* **25**, 948 (1967).
48. S.R. Kel'ner and Yu.D. Kotov, *Sov. J. Nucl. Phys.* **7**, 237 (1968).
49. R.P. Kokoulin and A.A. Petrukhin, in *Proceedings of the International Conference on Cosmic Rays*, Hobart, Australia, August 16–25, 1971, Vol. 4, p. 2436.
50. A.I. Nikishov, *Sov. J. Nucl. Phys.* **27**, 677 (1978).
51. Y.M. Andreev *et al.*, *Phys. Atom. Nucl.* **57**, 2066 (1994).
52. L.B. Bezrukov and E.V. Bugaev, *Sov. J. Nucl. Phys.* **33**, 635 (1981).
53. N.V. Mokhov, J.D. Cossairt, *Nucl. Instrum. Methods* **A244**, 349 (1986);
N.V. Mokhov, *Soviet J. Particles and Nuclei* (Sept.–Oct. 1987) 408–426;
N.V. Mokhov, "The MARS Code System User's Guide, Version 13(95)," Fermilab-FN-628, (April 1995).
54. L.B. Bezrukov and E.V. Bugaev, *Sov. J. Nucl. Phys.* **33**, 635 (1981).
55. A. Van Ginneken, *Nucl. Instrum. Methods* **A251**, 21 (1986).
56. U. Becker *et al.*, *Nucl. Instrum. Methods* **A253**, 15 (1986).
57. J.J. Eastman and S.C. Loken, in *Proceedings of the Workshop on Experiments, Detectors, and Experimental Areas for the Supercollider*, Berkeley, CA, July 7–17, 1987, edited by R. Donaldson and M.G.D. Gilchriese (World Scientific, Singapore, 1988), p. 542.
58. *Methods of Experimental Physics*, L.C.L. Yuan and C.-S. Wu, editors, Academic Press, 1961, Vol. 5A, p. 163.
59. W.W.M. Allison and P.R.S. Wright, "The Physics of Charged Particle Identification: dE/dx , Čerenkov Radiation, and Transition Radiation," p. 371 in *Experimental Techniques in High Energy Physics*, T. Ferbel, editor, (Addison-Wesley 1987).
60. E.R. Hayes, R.A. Schluter, and A. Tamosaitis, "Index and Dispersion of Some Čerenkov Counter Gases," ANL-6916 (1964).
61. T. Ypsilantis, "Particle Identification at Hadron Colliders", CERN-EP/89-150 (1989), or ECFA 89-124, **2** 661 (1989).